Journal of Statistical Mechanics: Theory and Experiment
An IOP and SISSA journal

PAPER: Classical statistical mechanics, equilibrium and non-equilibrium

Finite-time fluctuation theorem for diffusion-influenced surface reactions on spherical and Janus catalytic particles

Pierre Gaspard[1], **Patrick Grosfils**[1], **Mu-Jie Huang**[2] **and Raymond Kapral**[2]

[1] Center for Nonlinear Phenomena and Complex Systems, Université Libre de Bruxelles (U.L.B.), Code Postal 231, Campus Plaine, B-1050 Brussels, Belgium
[2] Chemical Physics Theory Group, Department of Chemistry, University of Toronto, Toronto, Ontario M5S 3H6, Canada
E-mail: gaspard@ulb.ac.be, Patrick.Grosfils@ulb.ac.be, mjhuang@chem.utoronto.ca and rkapral@chem.utoronto.ca

Received 17 July 2018
Accepted for publication 26 October 2018
Published 7 December 2018

Online at stacks.iop.org/JSTAT/2018/123206
https://doi.org/10.1088/1742-5468/aaeda1

J. Stat. Mech. (2018) 123206

Abstract. A finite-time fluctuation theorem for the diffusion-influenced surface reaction $A \rightleftharpoons B$ is investigated for spherical and Janus catalytic particles. The finite-time rates and thermodynamic force are analytically calculated by solving diffusion equations with the special boundary conditions of the finite-time fluctuation theorem. Theory is compared with numerical simulations carried out with two different methods: a random walk algorithm and multiparticle collision dynamics.

Keywords: chemical kinetics, fluctuation phenomena, large deviations in non-equilibrium systems, stochastic processes

1742-5468/18/123206+22$33.00

Contents

J. Stat. Mech. (2018) 123206

1. Introduction

Away from equilibrium, currents of energy and matter flow across open systems. Because of the atomic structure of matter, these currents manifest fluctuations, which can be characterized by their large-deviation properties within the framework of probability theory. Furthermore, the motions of microscopic particles obey fundamental time-reversal symmetry, which implies that the current fluctuations satisfy the so-called fluctuation theorems [1–15]. These theorems are usually obtained in the long-time limit. Remarkably, fluctuation theorems may also hold at every finite time under specific conditions. This is the case for Markov jump processes describing linear reactions in homogeneous systems [16]. Recently, a finite-time fluctuation theorem was established for diffusion-influenced surface reactions in spatially extended systems described by stochastic partial differential equations [17].

Fluctuation theorems play a key role in the determination of the thermodynamic forces driving systems into nonequilibrium steady states. Under such circumstances, the measurement of the driving forces is carried out in the long-time limit. In systems where a finite-time fluctuation theorem holds, the driving forces are defined at every finite time, and this allows one to understand how they vary in time and to determine the time scale on which they converge to their asymptotic values.

The purpose of this paper is to investigate aspects of the finite-time fluctuation theorem for the diffusion-influenced surface reaction $\mathrm{A} \rightleftharpoons \mathrm{B}$ on spherical and Janus catalytic particles. We deduce analytical expressions for the time dependence of the thermodynamic force of the reactive process by solving macroscopic diffusion equations with the special boundary conditions obtained in [17] and specified in detail in the next section. This solution provides the large-deviation properties of the random number of reactive events occurring during finite-time intervals.

The physical systems to which our analysis applies are catalytic colloidal particles either immobilized or suspended in a solution that contains reactive solute species whose concentrations far from the catalytic particles are fixed at specified values by reservoirs to establish a nonequilibrium steady state. The time-dependent affinity can be determined from measurements of the average value and variance of the net number of reactions that produce product in time intervals $[0, t]$ with the system maintained in the steady state. The theory applies to a fixed colloidal particle in solution; however, even if this is not the case in experiments, since colloidal particles are typically much larger than the molecular-scale solute and solvent particles, their motion is small and negligible, and comparisons with the theory that assumes immobile catalytic particles can be made. This is even true for self-propelled Janus motors provided their velocity is not too large to lead to significant violations of the theoretical conditions.

The theoretical results are compared with numerical simulations carried out using two different methods. In the first method, we consider a fixed spherical colloidal particle where the solute dynamics is simulated with particles carrying a color (A or B) and independently diffusing according to a random walk algorithm between the reservoir and the colloid catalytic surface where they may interchange their color. In the second method, the simulation is performed using multiparticle collision dynamics [18]. In this method, the system comprises reactive and solvent particles, together with a spherical composite catalytic particle made from a collection of linked beads [19], some of which catalyze the reaction $\mathrm{A} \rightleftharpoons \mathrm{B}$. Here the colloidal particle is not fixed but may diffuse in solution but its motion is slow on the scale of the diffusive solute dynamics and the theory is applicable for the reasons noted above.

The paper is organized as follows. The principal results of the finite-time fluctuation theorem are summarized in section 2. The theory is applied to a spherical catalytic particle in section 3, and a Janus catalytic particle in section 4. In these sections, the deterministic diffusion equations are solved for the geometries of the particles in these systems. Complete analytic expressions are obtained for the time dependence of the rates and the corresponding affinity. For each system, theory is compared with numerical simulations. Section 5 gives concluding remarks and perspectives.

2. The finite-time fluctuation theorem

We consider a system where the molecular species A and B diffuse in a three-dimensional domain V extending between three surfaces $\partial V = S_{\rm cat} \cup S_{\rm inert} \cup S_{\rm res}$. The reaction $\mathrm{A} \rightleftharpoons \mathrm{B}$ takes place at the catalytic surface $S_{\rm cat}$. The molecules A and B are reflected at the inert surface $S_{\rm inert}$. Moreover, they enter and exit the domain V at the surface $S_{\rm res}$ in contact with a reservoir. Accordingly, the concentrations (i.e. the densities) c_k of the species $k \in \{\mathrm{A}, \mathrm{B}\}$ are ruled by the fluctuating diffusion equations

$$\partial_t \, c_k + \boldsymbol{\nabla}\cdot\mathbf{j}_k = 0 \, , \qquad \text{with} \qquad \mathbf{j}_k = -D_k \boldsymbol{\nabla} c_k + \boldsymbol{\eta}_k \, , \tag{1}$$

and the boundary conditions

$$\text{if } \mathbf{r}\in S_{\rm cat} : \qquad D_{\rm A}\,\partial_\perp c_{\rm A}(\mathbf{r},t) = -D_{\rm B}\,\partial_\perp c_{\rm B}(\mathbf{r},t) = \kappa_+ c_{\rm A}(\mathbf{r},t) - \kappa_- c_{\rm B}(\mathbf{r},t) + \xi(\mathbf{r},t)\, , \tag{2}$$

$$\text{if } \mathbf{r}\in S_{\rm inert} : \qquad \partial_\perp c_k(\mathbf{r},t) = 0\, , \tag{3}$$

$$\text{if } \mathbf{r}\in S_{\rm res} : \qquad c_k(\mathbf{r},t) = \bar{c}_k \, , \tag{4}$$

where D_k are the diffusion coefficients, $\partial_\perp$ is the gradient in the direction normal to the surface and oriented towards the interior of the domain V, $\kappa_\pm$ are the surface reaction rate constants, and $\bar{c}_k$ the concentration values at the reservoir. The Gaussian noises associated with bulk diffusion are characterized by

$$\langle \boldsymbol{\eta}_k(\mathbf{r},t)\rangle = 0\, , \qquad \langle \boldsymbol{\eta}_k(\mathbf{r},t)\otimes\boldsymbol{\eta}_{k'}(\mathbf{r}',t')\rangle = 2\,D_k\,c_k(\mathbf{r},t)\,\delta_{kk'}\,\delta(\mathbf{r}-\mathbf{r}')\,\delta(t-t')\,\mathbf{1}\, , \tag{5}$$

with $k, k' \in \{{\rm A},{\rm B}\}$ and the 3×3 identity matrix $\mathbf{1}$, while the Gaussian noise associated with surface reaction satisfies

$$\langle \xi(\mathbf{r},t)\rangle = 0\, , \qquad \delta^{\rm s}(\mathbf{r})\,\langle \xi(\mathbf{r},t)\,\xi(\mathbf{r}',t')\rangle\,\delta^{\rm s}(\mathbf{r}') = (\kappa_+ c_{\rm A} + \kappa_- c_{\rm B})\,\delta^{\rm s}(\mathbf{r})\,\delta(\mathbf{r}-\mathbf{r}')\,\delta(t-t')\, , \tag{6}$$

where $\delta^{\rm s}(\mathbf{r})$ is the surface delta distribution, which is nonvanishing if $\mathbf{r}\in S_{\rm cat}$ [20].

We consider the probability $P(n,t)$ that the net number n of reactive events A → B have occurred during the time interval $[0,t]$ for the process evolving under stationary conditions with fixed boundary concentrations $\bar{c}_{\rm A}$ and $\bar{c}_{\rm B}$ at the reservoir. As proved in [17], this probability distribution satisfies the finite-time fluctuation theorem

$$\boxed{\frac{P(n,t)}{P(-n,t)} = \exp(\mathcal{A}_t\, n)} \tag{7}$$

at every time. What is remarkable about this result is that the ratio of the probabilities of opposite fluctuations is *exactly* given by an exponential function of n, despite of the nonGaussian character of the probability distribution $P(n,t)$ [17]. Here, the coefficient $\mathcal{A}_t$—usually referred to as the affinity—depends on time and takes the form

$$\mathcal{A}_t = \ln \frac{W_t^{(+)}}{W_t^{(-)}} \tag{8}$$

where $W_t^{(\pm)}$ are the time-dependent rates of the transitions $n\to n\pm 1$ in the counting statistics of reactive events during the time interval $[0,t]$. In [17], these rates are shown to have the analytical expressions

$$W_t^{(\pm)} = W_\infty^{(\pm)} + \frac{1}{t}\,\Psi(t)\, , \tag{9}$$

where their asymptotic values are given by

$$W_\infty^{(+)} = \Sigma\kappa_+\bar{c}_{\rm A}\, , \qquad\qquad W_\infty^{(-)} = \Sigma\kappa_-\bar{c}_{\rm B}\, , \tag{10}$$

and their time dependence by the function

$$\Psi(t) = \ell^2 \kappa_+ \kappa_- \left[\frac{\bar{c}_{\rm B}}{D_{\rm A}^2} \Upsilon_{\rm A}(t) + \frac{\bar{c}_{\rm A}}{D_{\rm B}^2} \Upsilon_{\rm B}(t) \right] . \tag{11}$$

The asymptotic values (10) of the rates can be calculated by expressing the stationary concentration fields for $k = {\rm A}, {\rm B}$ as

$$\langle c_k \rangle_{\rm st} = \bar{c}_k + \frac{\nu_k \ell}{D_k} \left(\kappa_+ \bar{c}_{\rm A} - \kappa_- \bar{c}_{\rm B} \right) \phi \, , \tag{12}$$

where $\nu_{\rm A} = -1$ and $\nu_{\rm B} = +1$ are the stoichiometric coefficients of the surface reaction and ϕ is the solution of the Laplace equation,

$$\nabla^2 \phi = 0 \, , \tag{13}$$

with the boundary conditions

$$(\partial_\perp \phi)_{\rm cat} = \ell^{-1} (\phi - 1)_{\rm cat} \, , \qquad (\partial_\perp \phi)_{\rm inert} = 0 \, , \qquad \text{and} \qquad (\phi)_{\rm res} = 0 \, , \tag{14}$$

involving the characteristic length of the diffusion-influenced surface reaction,

$$\ell \equiv \left(\frac{\kappa_+}{D_{\rm A}} + \frac{\kappa_-}{D_{\rm B}} \right)^{-1} . \tag{15}$$

The calculation carried out in [17] gives the results (10) expressed in terms of the effective catalytic surface area,

$$\Sigma = \int_{\rm cat} {\rm d}S \, (1 - \phi) \, . \tag{16}$$

As shown in [17], the time-dependent contribution (11) to the rates (9) can be obtained by solving the diffusion equations,

$$\partial_t f_k = D_k \nabla^2 f_k \, , \tag{17}$$

with the boundary and initial conditions

$$(\partial_\perp f_k)_{\rm cat} = \left(\frac{\kappa_+}{D_{\rm A}} f_{\rm A} + \frac{\kappa_-}{D_{\rm B}} f_{\rm B} \right)_{\rm cat} , \qquad (\partial_\perp f_k)_{\rm inert} = 0 \, , \qquad (f_k)_{\rm res} = 0 \, , \qquad (f_k)_{t=0} = \phi \, , \tag{18}$$

for $k = {\rm A}, {\rm B}$. By integration over the volume V of the system, the solutions f_k give the time-dependent functions

$$\Upsilon_k(t) = \int {\rm d}V \, \phi({\bf r}) \left[\phi({\bf r}) - f_k({\bf r}, t) \right] \, , \tag{19}$$

entering the expression (11). In this way, we can determine the probability distribution $P(n, t)$ and establish the finite-time fluctuation theorem (7) [17].

In the long-time limit, the finite-time affinity (8) converges to the value

$$\mathcal{A}_\infty = \ln \frac{W_\infty^{(+)}}{W_\infty^{(-)}} = \ln \frac{\kappa_+ \bar{c}_{\rm A}}{\kappa_- \bar{c}_{\rm B}} , \tag{20}$$

J. Stat. Mech. (2018) 123206

https://doi.org/10.1088/1742-5468/aaeda1

which is the control parameter for driving the system away from equilibrium. Indeed, thermodynamic equilibrium happens if $\kappa_+\bar{c}_{\rm A} = \kappa_-\bar{c}_{\rm B}$, in which case the affinity (20) is equal to zero. The mean current, i.e. the mean net reaction rate, is given by

$$\mathcal{J} = W_t^{(+)} - W_t^{(-)} = \Sigma\left(\kappa_+\bar{c}_{\rm A} - \kappa_-\bar{c}_{\rm B}\right) , \tag{21}$$

which does not depend on time because of the expression (9) for the rates. The mean net reaction rate can be written as

$$\mathcal{J} = \Sigma\kappa_-\bar{c}_{\rm B}\left(\exp\mathcal{A}_\infty - 1\right) \tag{22}$$

in terms of the control parameter (20) of the nonequilibrium steady state. However, the diffusivity of the current fluctuations

$$\mathcal{D}_t = \frac{1}{2}\left(W_t^{(+)} + W_t^{(-)}\right) = \frac{\Sigma}{2}\left(\kappa_+\bar{c}_{\rm A} + \kappa_-\bar{c}_{\rm B}\right) + \frac{1}{t}\,\Psi(t) \tag{23}$$

has a time dependence coming from the function (11). This time dependence arises from the fact that the counting statistics of the reactive events depends not only on the state of the system at the initial time $t=0$ when the statistics starts, but also on the time interval $[0, t]$, over which the statistics is carried on. In this regard, we note that the rates (9) are determined at early times by the stationary solutions (12) according to

$$W_t^{(+)} = \int_{\rm cat} {\rm d}S\,\kappa_+\langle c_{\rm A}\rangle_{\rm st} + O(t)\,, \tag{24}$$

$$W_t^{(-)} = \int_{\rm cat} {\rm d}S\,\kappa_-\langle c_{\rm B}\rangle_{\rm st} + O(t)\,. \tag{25}$$

However, the counting at longer times is conditioned not only by the initial state, but also by the number of reactive events that have occurred since the beginning of the counting. Consequently, the finite-time rates change depending on the diffusive transport associated with the reactive events during the time interval $[0, t]$, as described by equations (17) and (18).

As schematically depicted in figure 1, the probability distributions $P(\pm n, t)$ shift in opposite directions under nonequilibrium conditions, because their mean values are given by $\langle n\rangle_t = \pm\mathcal{J}t$ in terms of the mean current (21). Defining the entropy production rate of the counting statistics in terms of the Kullback–Leibler divergence between the probability distributions $P(\pm n, t)$, we find that it is given by ${\rm d_i}S/{\rm d}t = k_{\rm B}\mathcal{J}\mathcal{A}_t$, which converges in the long-time limit towards the expected entropy production rate of the reactive process, $k_{\rm B}\mathcal{J}\mathcal{A}_\infty$ [17]. If the concentrations at the reservoir satisfy the equilibrium condition, we have that $\mathcal{A}_\infty = 0$, so that the entropy production rate vanishes together with the mean net reaction rate (22). Detailed balance is thus recovered at equilibrium.

In the following sections, these results, proved in [17], are applied to spherical and Janus catalytic particles.

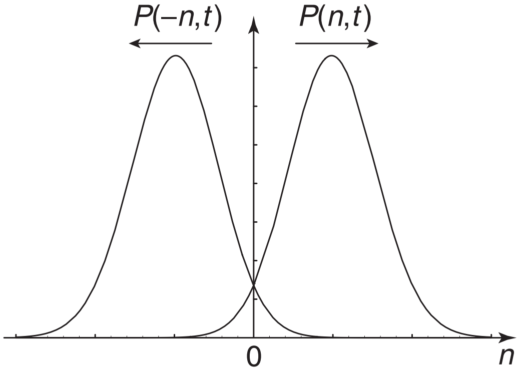

Figure 1. Schematic representation of the probability distributions $P(\pm n, t)$ of opposite fluctuations in the number n of reactive events occurring during the time interval $[0, t]$ under nonequilibrium conditions. These distributions shift away from the origin $n = 0$ as time t increases, so that their overlap rapidly decreases.

3. Spherical catalytic particle

3.1. Theory

We consider a spherical catalyst of radius $r = R$ centered on the origin of the reference frame, and a reservoir for species A and B that is located at a sphere of radius $r = L \gg R$, r denoting the radial distance from the origin. For this spherical geometry, the Laplacian operator in the problem (13) and (14) for the stationary solution reduces to

$$\nabla^2 \phi = \frac{1}{r} \frac{\mathrm{d}^2}{\mathrm{d}r^2} (r\, \phi) = 0\,, \tag{26}$$

while $\partial_\perp = \mathrm{d}/\mathrm{d}r$. Hence, the equations can be solved by setting $\phi(r) = u(r)/r$, yielding the solution

$$\phi(r) = R\, \frac{\mathrm{Da}}{\tilde{\Delta}} \left(\frac{1}{r} - \frac{1}{L} \right), \tag{27}$$

where

$$\mathrm{Da} \equiv \frac{R}{\ell} = R \left(\frac{\kappa_+}{D_\mathrm{A}} + \frac{\kappa_-}{D_\mathrm{B}} \right) \tag{28}$$

is the Damköhler number defined in terms of the characteristic length (15), and

$$\tilde{\Delta} \equiv 1 + \mathrm{Da} \left(1 - \frac{R}{L} \right). \tag{29}$$

The effective catalytic surface area (16) is given by $\Sigma = 4\pi R^2/\tilde{\Delta} = 4\pi R^2/[1 + \mathrm{Da} \times (1 - R/L)]$. Setting $f_k(r, t) = v_k(r, t)/r$, the functions (19) can be expressed as

$$\Upsilon_k(t) = 4\pi \int_R^L \mathrm{d}r\, u(r)\, [u(r) - v_k(r, t)]\,. \tag{30}$$

The solutions of equations (17) and (18) can be expanded as

$$v_k(r,t) = \sum_{i=1}^{\infty} a_i\, \mathrm{e}^{-D_k q_i^2 t} \sin q_i(L-r) + \chi_k \sum_{i=1}^{\infty} \tilde{a}_i\, \mathrm{e}^{-D_k \tilde{q}_i^2 t} \sin \tilde{q}_i(L-r) \tag{31}$$

with the coefficients $\chi_{\rm A} = D_{\rm A}/\kappa_+$ and $\chi_{\rm B} = -D_{\rm B}/\kappa_-$ and where the eigenvalues are the roots of

$$q_i R = -\Delta\, \tan q_i(L-R)\,, \tag{32}$$

$$\tilde{q}_i R = -\tan \tilde{q}_i(L-R)\,, \tag{33}$$

with $\Delta \equiv 1 + {\rm Da} = \lim_{L\to\infty} \tilde{\Delta}$ and $q_i, \tilde{q}_i > 0$. Since the solutions (31) satisfy the initial conditions $v_k(r, t = 0) = u(r)$ for $k = {\rm A}\,,{\rm B}$, we find that the expansion coefficients are given by

$$a_i = \frac{4R^2\left[\sin q_i(L-R) - q_i(L-R)\cos q_i(L-R)\right]}{q_i L \ell \tilde{\Delta}\left[2q_i(L-R) - \sin 2q_i(L-R)\right]} \tag{34}$$

and $\tilde{a}_i = 0$. Using equation (32), the functions (19) are obtained as

$$\Upsilon_k(t) = \frac{8\pi R^2}{\ell^2(L-R)} \sum_{i=1}^{\infty} \frac{1 - \mathrm{e}^{-D_k q_i^2 t}}{q_i^2\left[q_i^2 + \frac{\Delta\tilde{\Delta}}{R^2(1-R/L)}\right]}\,. \tag{35}$$

Therefore, the rates are given by equation (9) with

$$W_\infty^{(+)} = \frac{4\pi R^2}{\tilde{\Delta}}\, \kappa_+ \bar{c}_{\rm A}\,, \qquad W_\infty^{(-)} = \frac{4\pi R^2}{\tilde{\Delta}}\, \kappa_- \bar{c}_{\rm B}\,, \tag{36}$$

and

$$\Psi(t) = \frac{4\pi R^5 \kappa_+ \kappa_-}{\left(\Delta\tilde{\Delta}\right)^{3/2}} \left(1 - \frac{R}{L}\right)^{3/2} \left[\frac{\bar{c}_{\rm B}}{D_{\rm A}^2}\, \Omega_{\rm s}\left(\gamma_{\rm A} t\right) + \frac{\bar{c}_{\rm A}}{D_{\rm B}^2}\, \Omega_{\rm s}\left(\gamma_{\rm B} t\right)\right] \tag{37}$$

with the function

$$\Omega_{\rm s}(\tau) \equiv \frac{2R}{L\sqrt{\Delta\tilde{\Delta}(1-R/L)}} \sum_{i=1}^{\infty} \frac{1 - \mathrm{e}^{-Q_i^2 \tau}}{Q_i^2\left(Q_i^2 + 1\right)} \tag{38}$$

obtained after the substituting $Q_i = q_i R\sqrt{(L-R)/(L\Delta\tilde{\Delta})}$ and defining the rates

$$\gamma_k \equiv \frac{D_k \Delta\tilde{\Delta}}{R^2\left(1 - R/L\right)}\,. \tag{39}$$

Using these results, $\Psi(t)$ can be determined by numerical evaluation of the sums.

Using the long-time limit of equations (30) and (31), we find that the function (11) is given by

$$\Psi(\infty) = \frac{4\pi R^4 L \kappa_+ \kappa_-}{3\tilde{\Delta}^2} \left(1 - \frac{R}{L}\right)^3 \left(\frac{\bar{c}_{\rm A}}{D_{\rm B}^2} + \frac{\bar{c}_{\rm B}}{D_{\rm A}^2}\right). \tag{40}$$

We see that this asymptotic value is proportional to the distance L to the reservoir and thus diverges in the limit $L \to \infty$. Comparing equation (40) with the limit $t \to \infty$ of equation (37), we get

$$\Omega_{\rm s}(\infty) = \frac{L\Delta^{3/2}}{3R\tilde{\Delta}^{1/2}}\left(1 - \frac{R}{L}\right)^{3/2} . \tag{41}$$

Consequently, on the long time scale $D_k^{-1}L^2 \ll t$ for $k \in \{{\rm A}, {\rm B}\}$, the finite-time affinity behaves as

$$\mathcal{A}_t = \ln \frac{\kappa_+\bar{c}_{\rm A} + \frac{1}{t}\frac{R^2L\kappa_+\kappa_-}{3\tilde{\Delta}}\left(1-\frac{R}{L}\right)^3\left(\frac{\bar{c}_{\rm A}}{D_{\rm B}^2} + \frac{\bar{c}_{\rm B}}{D_{\rm A}^2}\right) + O\left(t^{-1}{\rm e}^{-D_{\rm A}q_1^2t}\right) + O\left(t^{-1}{\rm e}^{-D_{\rm B}q_1^2t}\right)}{\kappa_-\bar{c}_{\rm B} + \frac{1}{t}\frac{R^2L\kappa_+\kappa_-}{3\tilde{\Delta}}\left(1-\frac{R}{L}\right)^3\left(\frac{\bar{c}_{\rm A}}{D_{\rm B}^2} + \frac{\bar{c}_{\rm B}}{D_{\rm A}^2}\right) + O\left(t^{-1}{\rm e}^{-D_{\rm A}q_1^2t}\right) + O\left(t^{-1}{\rm e}^{-D_{\rm B}q_1^2t}\right)} . \tag{42}$$

In most experimental situations $L \gg R$, and in this case, the rates (36) take the well-defined values

$$W_\infty^{(+)} = \frac{4\pi R^2}{1+{\rm Da}}\,\kappa_+\bar{c}_{\rm A} , \qquad W_\infty^{(-)} = \frac{4\pi R^2}{1+{\rm Da}}\,\kappa_-\bar{c}_{\rm B} , \tag{43}$$

while the time-dependent function (37) becomes

$$\Psi(t) = \frac{4\pi R^5\kappa_+\kappa_-}{(1+{\rm Da})^3}\left[\frac{\bar{c}_{\rm B}}{D_{\rm A}^2}\,\Omega\left(\gamma_{\rm A}t\right) + \frac{\bar{c}_{\rm A}}{D_{\rm B}^2}\,\Omega\left(\gamma_{\rm B}t\right)\right] , \tag{44}$$

where $\gamma_k = D_kR^{-2}(1+{\rm Da})^2$ and the function (38) is given by its integral approximation,

$$\Omega(\tau) = \frac{1}{\pi}\int_{-\infty}^{+\infty}\frac{1-{\rm e}^{-Q^2\tau}}{Q^2\left(1+Q^2\right)}\,{\rm d}Q = 2\sqrt{\frac{\tau}{\pi}} - 1 + {\rm e}^{\tau}\,{\rm erfc}(\sqrt{\tau}) . \tag{45}$$

This function has the following asymptotic expansion for $\tau \to \infty$

$$\Omega(\tau) = 2\sqrt{\frac{\tau}{\pi}} - 1 + \frac{1}{\sqrt{\pi\tau}} + O\left(\frac{1}{\tau^{3/2}}\right) , \tag{46}$$

and Taylor series around $\tau = 0$

$$\Omega(\tau) = \tau - \frac{4}{3\sqrt{\pi}}\,\tau^{3/2} + \frac{1}{2}\,\tau^2 - \frac{8}{15\sqrt{\pi}}\,\tau^{5/2} + O(\tau^3) . \tag{47}$$

Consequently, the function (44) increases without limit as $\sqrt{t}$. However, it is divided by the time t in the expression (9) for the rates, which thus have the well-defined values (43) in the long-time limit. In simulations of the dynamics, one may have to account for system finite-size effects and the validity of these asymptotic expressions must be tested in these situations, but the more general results should apply.

If $L \gg R$, on the intermediate time scale $D_k^{-1}R^2/(1+{\rm Da})^2 \ll t \ll D_k^{-1}L^2$, the rates have the following expressions

$$W_t^{(\pm)} = W_\infty^{(\pm)} + \frac{2}{\sqrt{\pi t}}\frac{4\pi R^4\kappa_+\kappa_-}{(1+{\rm Da})^2}\left(\frac{\bar{c}_{\rm A}}{D_{\rm B}^{3/2}} + \frac{\bar{c}_{\rm B}}{D_{\rm A}^{3/2}}\right) + O(t^{-1}) \tag{48}$$

in terms of their asymptotic values (43). Accordingly, the affinity behaves as

$$\mathcal{A}_t = \ln \frac{\kappa_+\bar{c}_{\rm A} + \frac{2}{\sqrt{\pi t}}\frac{R^2\kappa_+\kappa_-}{1+{\rm Da}}\left(\frac{\bar{c}_{\rm A}}{D_{\rm B}^{3/2}} + \frac{\bar{c}_{\rm B}}{D_{\rm A}^{3/2}}\right) + O(t^{-1})}{\kappa_-\bar{c}_{\rm B} + \frac{2}{\sqrt{\pi t}}\frac{R^2\kappa_+\kappa_-}{1+{\rm Da}}\left(\frac{\bar{c}_{\rm A}}{D_{\rm B}^{3/2}} + \frac{\bar{c}_{\rm B}}{D_{\rm A}^{3/2}}\right) + O(t^{-1})}. \tag{49}$$

In the long-time limit, the affinity (8) thus converges towards the expected asymptotic value (20).

On the short time scale $t \ll D_k^{-1}R^2/(1+{\rm Da})^2$, equations (24) and (25) with equation (12) show that the rates are given at early times by

$$\begin{aligned} W_t^{(+)} &= \frac{4\pi R^2\kappa_+}{\tilde{\Delta}}\left[\bar{c}_{\rm A} + \kappa_- R\left(1-\frac{R}{L}\right)\left(\frac{\bar{c}_{\rm A}}{D_{\rm B}} + \frac{\bar{c}_{\rm B}}{D_{\rm A}}\right)\right] + O(t)\,, \\ W_t^{(-)} &= \frac{4\pi R^2\kappa_-}{\tilde{\Delta}}\left[\bar{c}_{\rm B} + \kappa_+ R\left(1-\frac{R}{L}\right)\left(\frac{\bar{c}_{\rm A}}{D_{\rm B}} + \frac{\bar{c}_{\rm B}}{D_{\rm A}}\right)\right] + O(t)\,, \end{aligned} \tag{50}$$

and the corresponding affinity is

$$\mathcal{A}_t = \ln \frac{\kappa_+\bar{c}_{\rm A} + \kappa_+\kappa_- R\left(1-\frac{R}{L}\right)\left(\frac{\bar{c}_{\rm A}}{D_{\rm B}} + \frac{\bar{c}_{\rm B}}{D_{\rm A}}\right) + O(t)}{\kappa_-\bar{c}_{\rm B} + \kappa_+\kappa_- R\left(1-\frac{R}{L}\right)\left(\frac{\bar{c}_{\rm A}}{D_{\rm B}} + \frac{\bar{c}_{\rm B}}{D_{\rm A}}\right) + O(t)}\,, \tag{51}$$

which holds for small enough times. Therefore, the affinity can take an early-time value that is much smaller than its asymptotic value (20).

We notice that, according to equation (43), the mean rate is given in the limit $L \gg R$ by $\mathcal{J} = W_\infty^{(+)} - W_\infty^{(-)} = 4\pi R^2(\kappa_+\bar{c}_{\rm A} - \kappa_-\bar{c}_{\rm B})/(1+{\rm Da})$ for the spherical catalytic particle.

Taking equation (49) with $D = D_{\rm A} = D_{\rm B}$ and $\kappa = \kappa_\pm$, we see that the affinity reaches its asymptotic value if

$$t \gg \left(\frac{\rm Da}{{\rm Da}+1}\right)^2 \frac{R^2}{D}\,. \tag{52}$$

This condition reads $t \gg R^2/D$ in the diffusion-limited regime where ${\rm Da} \gg 1$, and $t \gg {\rm Da}^2 R^2/D$ in the reaction-limited regime where ${\rm Da} \ll 1$. The convergence time is thus shorter in the reaction-limited regime than in the diffusion-limited one. Since the molecular diffusivities typically take the value $D \simeq 10^{-9}$ m^2 s^{-1}, the convergence time for a catalytic particle of micrometric radius is of the order of milliseconds.

3.2. Numerical results

For the simulation results, we suppose that the diffusion coefficients and the forward and reverse rate constants are equal, $D \equiv D_{\rm A} = D_{\rm B}$ and $\kappa \equiv \kappa_\pm$. The function $\Psi(t)$ in equation (11) is given by

$$\Psi(t) = \frac{\ell^2\kappa^2}{D^2}\left(\bar{c}_{\rm A} + \bar{c}_{\rm B}\right)\,\Upsilon(t) \tag{53}$$

with

$$\Upsilon(t) = 4\pi \int_R^L \mathrm{d}r\, u(r)\, \left[u(r) - v(r,t)\right], \tag{54}$$

where $u(r) = \ell^{-1}\tilde{\Delta}^{-1}R^2\,(1 - r/L)$ and $\tilde{\Delta} \equiv 1 + 2\kappa D^{-1}R\,(1 - R/L)$. The function $v(r,t)$ is the solution of the following problem:

$$\partial_t v(r,t) = D\,\partial_r^2 v(r,t)\,, \tag{55}$$

$$R\,\partial_r v(R,t) = \left(1 + \frac{2\kappa R}{D}\right) v(R,t)\,, \tag{56}$$

$$v(L,t) = 0\,, \tag{57}$$

$$v(r,0) = u(r)\,, \tag{58}$$

which can be solved numerically by spatial discretization into I cells of size $\Delta r = (L - R)/I$.

These theoretical expressions are compared with numerical simulations based on a diffusive random walk model as well as multiparticle collision dynamics. These two particle-based simulation methods model the dynamics in different but complementary ways. In the random walk model, the dynamics of the solute A and B particles is described by overdamped Langevin equations, and encounters with the catalytic surface lead to reactions that change the identities of these species. The simulation of the random walk process is described in appendix A. In the multiparticle collision dynamics scheme, the solute and solvent species undergo effective collisions in a manner that preserves the basic conservation laws. The A and B particles interact with the colloid through repulsive Lennard-Jones intermolecular potentials and reactions again occur upon encounters with the catalytic surface. Simulation details for this method are given in appendix B, and further details of both methods and results are given below. The parameters in these methods may be chosen to study either the reaction-limited or diffusion-limited regimes.

We first discuss the results obtained when the A and B particles move according to a diffusive random walk process between a spherical catalytic particle of radius $r = R$ and an outer sphere of larger radius $r = L$ where the molecules have the fixed concentrations $\bar{c}_{\mathrm{A}}$ and $\bar{c}_{\mathrm{B}}$. The system contains a total of $N = 522\,909$ A and B particles with $r < L$. The parameters take the following values:

$$D = 1\,, \qquad \kappa = 0.4\,, \qquad R = 0.5\,, \qquad L = 5\,, \qquad \bar{c}_{\mathrm{A}} = 526.1169\,, \qquad \bar{c}_{\mathrm{B}} = 473.5751\,. \tag{59}$$

The process is at the crossover between the reaction- and diffusion-limited regimes because $\mathrm{Da} = 2\kappa R/D = 0.4$ and $\tilde{\Delta} = 1 + \mathrm{Da}\,(1 - R/L) = 1.36$. The mean reaction rate is $\mathcal{J} = 48.55$ and the zero-time properties are given by

$$W_0^{(+)} = 652.40\,, \qquad W_0^{(-)} = 603.85\,, \qquad \mathcal{D}_0 = 628.13\,, \qquad \mathcal{A}_0 = 0.077\,329\,, \tag{60}$$

while the asymptotic properties are

$$W_\infty^{(+)} = 486.13\,, \qquad W_\infty^{(-)} = 437.58\,, \qquad \mathcal{D}_\infty = 461.86\,, \qquad \mathcal{A}_\infty = 0.105\,21\,. \tag{61}$$

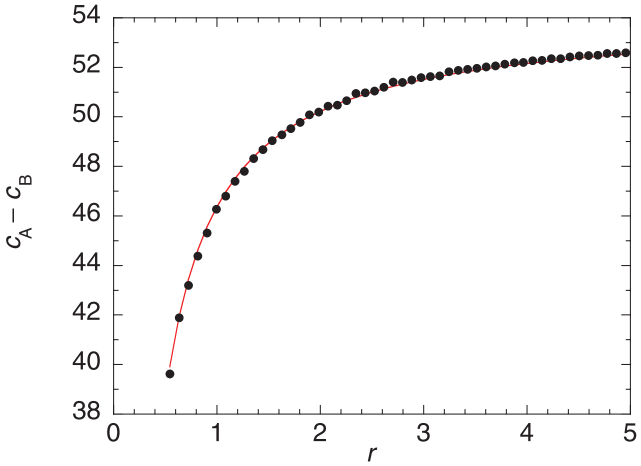

Figure 2. Spherical catalytic particle: stationary profile of the concentration difference $c_{\mathrm{A}} - c_{\mathrm{B}}$ versus the radial distance r for the simulation with the random walk algorithm and the parameter values (59). The dots are the simulation data and the solid line the theoretical result.

These theoretical values compare favorably with the computational results: $\mathcal{J} \simeq 49.7$ and $\mathcal{D}_\infty \simeq 465$. The stationary profile of the concentration difference $c_{\mathrm{A}} - c_{\mathrm{B}}$ is depicted in figure 2 and is in agreement with the theoretical expectation (27).

The finite-time affinity is shown in figure 3 where the computational results (squares) are compared with theory (solid line) obtained by spatial discretization into $I = 1000$ cells. The affinity is directly measured from simulation data as the slope of $\ln[P(n,t)/P(-n,t)]$ versus the number n of reactive events during the time interval $[0,t]$ (open squares with error bars). As time increases, the overlap between the probability distributions $P(n,t)$ and $P(-n,t)$ rapidly decreases. In order to overcome this difficulty, the Gaussian probability distribution

$$P(n,t) \simeq \frac{1}{\sqrt{2\pi\sigma_t^2}} \exp\left[-\frac{(n - \langle n\rangle_t)^2}{2\sigma_t^2}\right] \tag{62}$$

is fitted to the histogram. No significant deviations between the histogram and the Gaussian distribution have been observed. The affinity is thus estimated as $\mathcal{A}_t \simeq 2\,\langle n\rangle_t/\sigma_t^2$. These values are depicted as filled squares in figure 3, showing agreement between the simulation data and theory, given that the simulation overestimates the values of the mean rate $\mathcal{J}$ and thus the affinity $\mathcal{A}_\infty$ by about 2% with respect to theory.

As noted above, microscopic simulations have also been carried out using a hybrid molecular dynamics-multiparticle collision dynamics scheme [18, 21–23]. In particular, we use the implementation with reversible catalytic reactions that satisfies detailed balance [19]. The catalytic particle resides in a system containing half inert solvent (S) particles and half reactive A and B particles. The roughly spherical catalytic particle is made of catalytic (C) beads connected by stiff harmonic springs. The fluid species interact with the particle beads through repulsive Lennard-Jones potential functions. Reversible reactions, $\mathrm{C} + \mathrm{A} \rightleftharpoons \mathrm{C} + \mathrm{B}$, take place on the catalytic beads with forward (p_+) and reverse (p_-) reaction probabilities. The reactive collision rule is designed such that the forward and reverse collisions satisfy the principle of detailed balance.

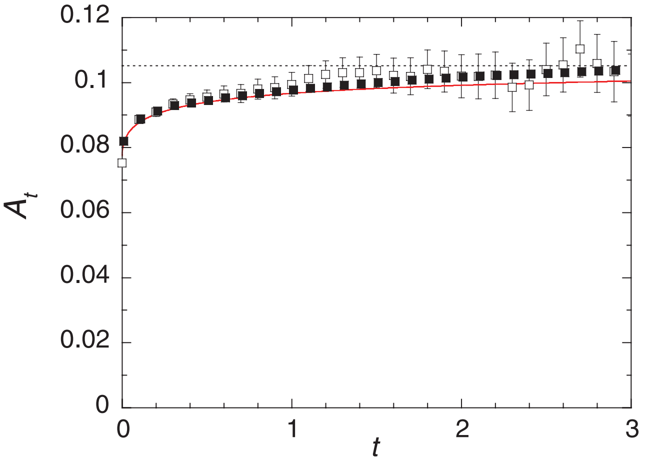

Figure 3. Spherical catalytic particle: affinity $\mathcal{A}_t$ versus time t for the simulation with the random walk algorithm and the parameter values (59). The squares are the simulation data and the solid line the theoretical result. The open squares show the affinity directly measured with $\ln[P(n,t)/P(-n,t)]$, while the filled squares show the affinity obtained from the Gaussian fit (62). The dashed line gives the asymptotic value of the affinity.

To establish nonequilibrium conditions, the concentrations of A and B particles at a distance L are controlled by relabelling particle species as A with probability $\bar{p}_{\rm A}$ or as B with probability $\bar{p}_{\rm B} = 1 - \bar{p}_{\rm A}$ when a reactive particle moves across the boundary at L from the region outside L into the system. The resulting concentrations at $r = L$ are $\bar{c}_{\rm A} = \bar{p}_{\rm A} c_0$ and $\bar{c}_{\rm B} = \bar{p}_{\rm B} c_0$, where $c_0 = \bar{c}_{\rm A} + \bar{c}_{\rm B}$ is the total concentration of A and B particles. This simulates a system where the concentrations outside of the sphere of radius L are prescribed to be $\bar{c}_{\rm A}$ and $\bar{c}_{\rm B}$. The spherical particle is not fixed in space and undergoes Brownian motion. The sphere of radius L is centered on the instantaneous position of the particle. This method requires the intermolecular potentials and multiparticle collision parameters, such as the collision time and collision rule, to be specified. The fluid transport properties including the solute diffusion coefficients and fluid viscosity then follow from the dynamics. For times long compared to the collision time, the solute species will exhibit diffusive motion, similar to that in the random walk model. The structure of the boundary layer is determined by intermolecular interactions between the colloid and fluid species. Consequently, it is of interest to compare the dynamics of this model with the theoretical predictions.

As above, we focus on the case where the diffusion coefficients and the forward and reverse rate constants are equal, $D \equiv D_{\rm A} = D_{\rm B}$ and $\kappa \equiv \kappa_{\pm}$. To determine $\kappa \equiv k^0/(4\pi R^2)$, we consider the irreversible reaction ${\rm C} + {\rm A} \to {\rm C} + {\rm B}$ on the particle with reaction probability $p_+ = 1$. The rate law for this case is ${\rm d}c_{\rm A}(t)/{\rm d}t = -k(t) n_{\rm C} c_{\rm A}(t)$, where $n_{\rm C} = 1/V$ is the colloidal particle density. The time-dependent rate coefficient $k(t)$ starts at $k(0^+) = k^0$ and decays to the asymptotic value $k = k^0 k_D/(k^0 + k_D)$ where $k_D = 4\pi D R$ is the diffusion-limited rate constant [19, 24]. The time-dependent rate coefficient can be found by computing $k(t) = -[{\rm d}c_{\rm A}(t)/{\rm d}t]/[n_{\rm C} c_{\rm A}(t)]$ with the system starting from all A particles in the bulk without particle relabelling at the boundary L. The values obtained are $k^0 \simeq 188.4 \pm 17.6$ and $k \simeq 3.68 \pm 0.05$, from which one gets $k_D \simeq 3.75$. From k_D, one can estimate the outer edge of boundary layer to be at

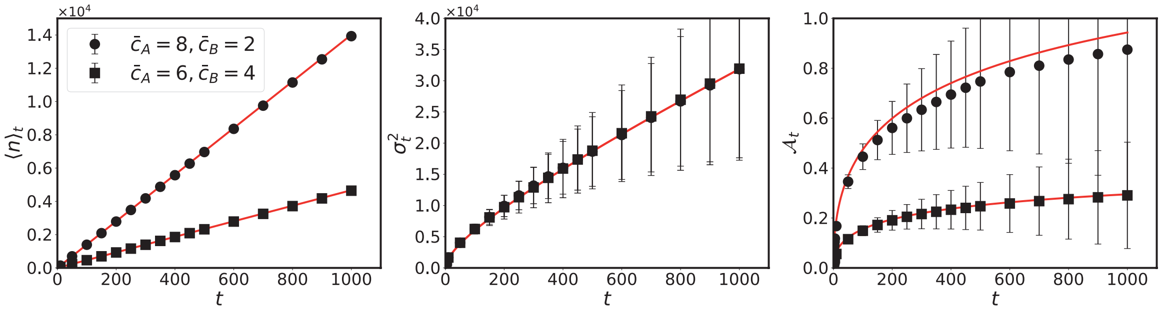

Figure 4. Spherical catalytic particle: plots of $\langle n \rangle_t$, σ_t^2 and the finite-time affinity $\mathcal{A}_t$ versus time t for two different reservoir conditions indicated in the figure inset. The dots and the squares are the simulation data of the multiparticle collision dynamics and the solid lines the theoretical results.

$R = k_D/(4\pi D) \simeq 5.0$, where $D = 0.0596$ is the fluid species diffusion coefficient. The Damköhler number is equal to $\mathrm{Da} = 2\kappa R/D \simeq 100$, and $\tilde{\Delta} = 80.2$, meaning that the system is in the diffusion-limited regime.

The following two sets of parameter values with different reservoir concentrations have been used to obtain the results:

$$D = 0.0596\,, \qquad \kappa = 0.6\,, \qquad R = 5.0\,, \qquad L = 24\,, \qquad \bar{c}_{\mathrm{A}} = \{8, 6\}\,, \qquad \bar{c}_{\mathrm{B}} = \{2, 4\}\,. \tag{63}$$

The mean reaction rates are $\mathcal{J} \simeq \{14.0, 4.7\}$, the zero-time properties are given by

$$W_0^{(+)} = \{941.7, 937.0\}\,,\ W_0^{(-)} = \{927.7, 932.4\}\,,\ \mathcal{D}_0 = \{934.7, 934.7\}\,,\ \mathcal{A}_0 = \{0.015, 0.005\}\,, \tag{64}$$

while the asymptotic properties are

$$W_\infty^{(+)} = \{18.7, 14.0\}\,,\ W_\infty^{(-)} = \{4.7, 9.3\}\,,\ \mathcal{D}_\infty = \{11.7, 11.7\}\,,\ \mathcal{A}_\infty = \{1.4, 0.4\}\,. \tag{65}$$

These theoretical values compare favorably with the computational results: $\mathcal{J} \simeq \{13.9, 4.6\}$ and $\mathcal{D}_\infty \simeq \{13.6, 13.2\}$. The time-dependent $\langle n \rangle_t$, σ_t^2 and $\mathcal{A}_t$ obtained from theory and simulations are plotted in figure 4 where good agreement is seen. We observe that a small few percent error in $\langle n \rangle_t$ is amplified in the estimate of $\mathcal{A}_t$ and is responsible for the discrepancy between theory and simulation in the graph, although the results are still within the statistical errors.

Comparing figures 3 and 4, we observe that the time-dependent affinity $\mathcal{A}_t$ starts from an early-time value $\mathcal{A}_0$ that is much closer to the asymptotic value $\mathcal{A}_\infty$ in the reaction-limited regime than in the diffusion-limited regime. The reason is that the time-dependent affinity converges faster in the former regime than in the latter regime, as shown in section 3.1 with equation (52).

4. Janus catalytic particle

Janus catalytic particles, where one hemisphere is catalytically active while the other is not, are often studied in the laboratory, especially when they can act as motors propelled by phoretic mechanisms. When such motors are pinned in solution they can act as fluid pumps. The asymmetry of the catalytic activity also introduces new features in the finite-time fluctuation theorem results and for these reasons it is interesting to extend our considerations to such colloidal catalytic particles.

4.1. Theory

Here, we consider an immobile Janus particle of radius R centered on the origin $r = 0$ in the spherical coordinates (r, θ, φ). The upper hemisphere is catalytic and the lower one is inert, so that the problem has a cylindrical symmetry under the rotations $\varphi \to \varphi + \alpha$ around the axis of the Janus particle.

The stationary problem (13) and (14) is given by

$$\nabla^2 \phi = \frac{1}{r}\frac{\partial^2}{\partial r^2}(r\,\phi) + \frac{\hat{\mathcal{L}}}{r^2}\,\phi = 0\,, \tag{66}$$

with the operator acting as $\hat{\mathcal{L}} Y_{lm} = -l(l+1) Y_{lm}$ on the spherical harmonics $Y_{lm}(\theta, \varphi)$. The boundary conditions read

$$\left(\frac{\partial \phi}{\partial r}\right)_R = \frac{1}{\ell}(\phi - 1)_R H(\cos\theta) \qquad \text{and} \qquad (\phi)_L = 0\,, \tag{67}$$

where $H(\xi)$ is Heaviside's function such that $H(\xi) = 1$ if $\xi = \cos\theta > 0$ and zero otherwise. The solution of this problem can be expressed as

$$\phi(r,\theta) = \mathrm{Da} \sum_{l=0}^{\infty} a_l \left[\left(\frac{R}{r}\right)^{l+1} - \left(\frac{R}{L}\right)^{l+1}\left(\frac{r}{L}\right)^{l}\right] P_l(\cos\theta) \tag{68}$$

in terms of the coefficients

$$a_l = \sum_{l'=0}^{\infty} (\mathbf{M}^{-1})_{ll'} \int_0^1 \mathrm{d}\xi\, P_{l'}(\xi) \tag{69}$$

with

$$(\mathbf{M})_{ll'} = \frac{2}{2l+1}\left[l+1+l\left(\frac{R}{L}\right)^{2l+1}\right]\delta_{ll'} + \mathrm{Da}\left[1 - \left(\frac{R}{L}\right)^{2l'+1}\right]\int_0^1 \mathrm{d}\xi\, P_l(\xi)\, P_{l'}(\xi)\,, \tag{70}$$

where Da is the Damköhler number (28). The stationary mean concentrations are thus given by equation (12).

Here, the effective catalytic surface area (16) is given by $\Sigma = 4\pi R^2 a_0 = 2\pi R^2 \times (1 - \mathrm{Da}\,\gamma_{\mathrm{J}})$ with the constant

$$\gamma_{\mathrm{J}} = \frac{1-2a_0}{\mathrm{Da}} = \sum_{l=0}^{\infty} a_l \left[1 - \left(\frac{R}{L}\right)^{2l+1}\right] \int_0^1 \mathrm{d}\xi\, P_l(\xi)\,. \tag{71}$$

In the limit $L \to \infty$, the effective catalytic surface area can be approximated by $\Sigma \simeq 2\pi R^2/(1 + 0.708\,115\,\mathrm{Da})$, as shown in [25].

The functions (19) can here be expressed as

$$\Upsilon_k(t) = 4\pi \int_R^L \mathrm{d}r \sum_{l=0}^{\infty} \frac{1}{2l+1}\, v_{kl}(r,0)\left[v_{kl}(r,0) - v_{kl}(r,t)\right], \tag{72}$$

by expanding the functions $f_k(r,\theta,t)$ as

$$f_k(r,\theta,t) = \frac{1}{r}\sum_{l=0}^{\infty} v_{kl}(r,t)\, P_l(\cos\theta) \tag{73}$$

in terms of the solutions of

$$\partial_t v_{kl}(r,t) = D_k \left[\partial_r^2 - \frac{l(l+1)}{r^2}\right] v_{kl}(r,t) \tag{74}$$

with the boundary conditions

$$(\partial_r v_{kl})_R = \frac{1}{R}(v_{kl})_R + \frac{2l+1}{2}\sum_{l'=0}^{\infty}\left(\frac{\kappa_+}{D_{\rm A}}\, v_{{\rm A}l'} + \frac{\kappa_-}{D_{\rm B}}\, v_{{\rm B}l'}\right)_R \int_0^1 {\rm d}\xi\, P_l(\xi)\, P_{l'}(\xi) \tag{75}$$

and $(v_{kl})_L = 0$, and starting from the initial conditions

$$v_{kl}(r,0) = {\rm Da}\, R\, a_l \left[\left(\frac{R}{r}\right)^l - \left(\frac{R}{L}\right)^l \left(\frac{r}{L}\right)^{l+1}\right] \tag{76}$$

for $k = {\rm A}$ and $k = {\rm B}$.

Therefore, the rates are given by equation (9) with

$$W_\infty^{(+)} = 2\pi R^2\,(1 - {\rm Da}\,\gamma_{\rm J})\;\kappa_+\bar{c}_{\rm A}\,, \qquad W_\infty^{(-)} = 2\pi R^2\,(1 - {\rm Da}\,\gamma_{\rm J})\;\kappa_-\bar{c}_{\rm B}\,, \tag{77}$$

and the function (11) is expressed in terms of the functions (72), which behave qualitatively as in the spherical geometry. If L is finite, we have in the long-time limit that

$$\Upsilon_{\rm A}(\infty) = \Upsilon_{\rm B}(\infty) = \frac{4\pi}{3}\, a_0^2\, \frac{R^4}{\ell^2}\, L\,\left[1 + O(R/L)\right] \qquad \text{with} \qquad a_0 = \frac{1}{2}\,(1 - {\rm Da}\,\gamma_{\rm J})\,, \tag{78}$$

so that

$$\Psi(\infty) = \frac{4\pi}{3}\, a_0^2 R^4 L \kappa_+\kappa_- \left(\frac{\bar{c}_{\rm A}}{D_{\rm B}^2} + \frac{\bar{c}_{\rm B}}{D_{\rm A}^2}\right)\left[1 + O(R/L)\right], \tag{79}$$

which is proportional to L as in the spherical geometry. Therefore, the rates (9) converge to their asymptotic value (77) with corrections of $O(1/t)$, if L remains finite. However, if L is infinite, the convergence proceeds with corrections of $O(1/\sqrt{t})$, as in the spherical geometry. Consequently, the affinity (8) converges towards its asymptotic value (20) if L is finite and infinite.

According to equation (25), the rates are given at early time by

$$W_t^{(+)} = 2\pi R^2 \kappa_+ \left[\bar{c}_{\rm A} - \gamma_{\rm J}\, \frac{R}{D_{\rm A}}\,(\kappa_+\bar{c}_{\rm A} - \kappa_-\bar{c}_{\rm B})\right] + O(t)\,, \tag{80}$$

$$W_t^{(-)} = 2\pi R^2 \kappa_- \left[\bar{c}_{\rm B} + \gamma_{\rm J}\, \frac{R}{D_{\rm B}}\,(\kappa_+\bar{c}_{\rm A} - \kappa_-\bar{c}_{\rm B})\right] + O(t)\,, \tag{81}$$

so that the early time behavior of the affinity is given by

J. Stat. Mech. (2018) 123206

$$\mathcal{A}_t = \ln \frac{\kappa_+ \left[\bar{c}_{\rm A} - \gamma_{\rm J}\, \frac{R}{D_{\rm A}}\, (\kappa_+ \bar{c}_{\rm A} - \kappa_- \bar{c}_{\rm B})\right] + O(t)}{\kappa_- \left[\bar{c}_{\rm B} + \gamma_{\rm J}\, \frac{R}{D_{\rm B}}\, (\kappa_+ \bar{c}_{\rm A} - \kappa_- \bar{c}_{\rm B})\right] + O(t)}, \tag{82}$$

which can also be much smaller than the asymptotic affinity (20).

For the Janus catalytic particle, the mean rate is thus given in the limit $L \gg R$ by $\mathcal{J} = W_\infty^{(+)} - W_\infty^{(-)} \simeq 2\pi R^2 (\kappa_+ \bar{c}_{\rm A} - \kappa_- \bar{c}_{\rm B})/(1 + 0.708\,115\,{\rm Da})$.

4.2. Numerical results

We again suppose that the diffusion coefficients and the rate constants are equal, $D \equiv D_{\rm A} = D_{\rm B}$ and $\kappa \equiv \kappa_\pm$. The finite-time affinity is thus given by equation (8) with the rates

$$W_t^{(+)} = 2\pi R^2 \kappa\, (1 - {\rm Da}\, \gamma_{\rm J})\, \bar{c}_{\rm A} + \ell^2 \frac{\kappa^2}{D^2}\, (\bar{c}_{\rm A} + \bar{c}_{\rm B})\, \frac{\Upsilon(t)}{t}\,, \tag{83}$$

$$W_t^{(-)} = 2\pi R^2 \kappa\, (1 - {\rm Da}\, \gamma_{\rm J})\, \bar{c}_{\rm B} + \ell^2 \frac{\kappa^2}{D^2}\, (\bar{c}_{\rm A} + \bar{c}_{\rm B})\, \frac{\Upsilon(t)}{t}\,, \tag{84}$$

where the function $\Upsilon(t) = \Upsilon_{\rm A}(t) = \Upsilon_{\rm B}(t)$ is defined by equation (72) and calculated by solving equations (74) and (75) for $v_l(r,t) \equiv v_{{\rm A}l}(r,t) = v_{{\rm B}l}(r,t)$. This problem is solved numerically by spatial discretization $v_{l,i}(t) = v_l(r_i, t)$ with $r_i = R + (i - 1/2)\Delta r$ where $i = 1, 2, ..., I$ and $\Delta r = (L - R)/I$ with $I = 20$ and $l \leqslant 100$ (see details in appendix C).

Again, the theoretical results are compared with simulations where A and B particles move according to a diffusive random walk process between an immobile Janus particle of radius $r = R$ with a hemispherical catalytic surface and an outer sphere of larger radius $r = L$ where the molecules have the fixed concentrations $\bar{c}_{\rm A}$ and $\bar{c}_{\rm B}$, as described in appendix A. The system contains a total of $N = 523\,164$ A and B particles with $r < L$. Here, the parameters have the following values:

$$D = 1\,, \qquad \kappa = 0.4\,, \qquad R = 0.5\,, \qquad L = 5\,, \qquad \bar{c}_{\rm A} = 527.195\,, \qquad \bar{c}_{\rm B} = 474.545\,. \tag{85}$$

The process is at the crossover between the reaction- and diffusion-limited regimes since ${\rm Da} = 2\kappa R/D = 0.4$. For this system, we have that $\gamma_{\rm J} = 0.519\,60$. The mean reaction rate is given by $\mathcal{J} = 26.2$, the time-zero properties by

$$W_0^{(+)} = 327.81\,, \qquad W_0^{(-)} = 301.60\,, \qquad \mathcal{D}_0 = 314.71\,, \qquad \mathcal{A}_0 = 0.083\,318\,, \tag{86}$$

and the asymptotic properties by

$$W_\infty^{(+)} = 262.40\,, \qquad W_\infty^{(-)} = 236.19\,, \qquad \mathcal{D}_\infty = 249.30\,, \qquad \mathcal{A}_\infty = 0.105\,21\,. \tag{87}$$

Here also, these theoretical values compare favorably with the computational results: $\mathcal{J} \simeq 26.5$ and $\mathcal{D}_\infty \simeq 250$. We notice that the diffusivity does not deviate much from its asymptotic value in the present case.

The finite-time affinity is shown in figure 5 where the computational results (squares) are compared with theory (solid line). As for the spherical catalytic particle, the affinity is directly measured from simulation data as the slope of $\ln[P(n,t)/P(-n,t)]$ versus the number n of reactive events during the time interval $[0,t]$ (open squares with error

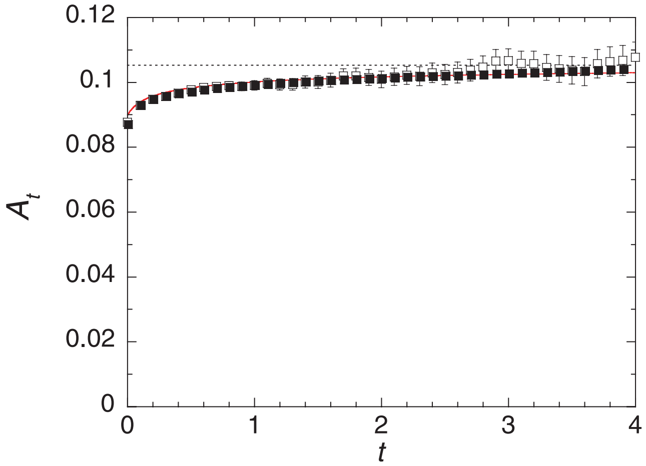

Figure 5. Janus catalytic particle: affinity $\mathcal{A}_t$ versus time t for the simulation with the random walk algorithm and the parameter values (85). The squares are the simulation data and the solid line the theoretical result. The open squares show the affinity directly measured with $\ln[P(n,t)/P(-n,t)]$, while the filled squares show the affinity obtained from the Gaussian fit (62). The dashed line gives the asymptotic value of the affinity.

bars), as well as by Gaussian fits to the histograms of n values. No significant deviations between the histogram and the Gaussian distribution have been observed. The affinity is then estimated as $\mathcal{A}_t \simeq 2\,\langle n\rangle_t/\sigma_t^2$. These values are depicted as filled squares in figure 5, showing here also agreement between the simulation data and theory.

Microscopic simulations as described in appendix B have also been carried out for a Janus particle made from catalytic and noncatalytic beads connected by stiff harmonic springs. We have chosen the interaction potentials of the A and B particles with the beads of the Janus particle to be equal so that the diffusiophoretic mechanism that leads to self propulsion does not operate. The Janus particle does, however, execute Brownian motion as is the case for the spherical particle. Again, we investigate the time-dependent reaction rates, diffusivities and affinity for two parameter sets with different reservoir concentrations:

$$D = 0.0596\,, \qquad \kappa = 0.6\,, \qquad R = 5.0\,, \qquad L = 24\,, \qquad \bar{c}_{\rm A} = \{8, 6\}\,, \qquad \bar{c}_{\rm B} = \{2, 4\}\,. \tag{88}$$

Here, the process evolves in the diffusion-limited regime because the Damköhler number has the value ${\rm Da} = 2\kappa R/D \simeq 100$. The mean reaction rates are $\mathcal{J} \simeq \{9.7, 3.23\}$, the zero-time properties are given by

$$W_0^{(+)} = \{475.8, 472.6\}\,,\ W_0^{(-)} = \{466.1, 469.4\}\,,\ \mathcal{D}_0 = \{471.0, 471.0\}\,,\ \mathcal{A}_0 = \{0.021, 0.0068\}\,, \tag{89}$$

while the asymptotic properties are

$$W_\infty^{(+)} = \{12.9, 9.7\}\,,\ W_\infty^{(-)} = \{3.23, 6.47\}\,,\ \mathcal{D}_\infty = \{8.09, 8.09\}\,,\ \mathcal{A}_\infty = \{1.38, 0.405\}\,. \tag{90}$$

These theoretical values compare favorably with the simulation results: $\mathcal{J} \simeq \{10.1, 3.35\}$ and $\mathcal{D}_\infty \simeq \{9.3, 10.6\}$. The time-dependent $\langle n\rangle_t$, σ_t^2 and $\mathcal{A}_t$ obtained from theory and simulations are plotted in figure 6 where good agreement is seen.

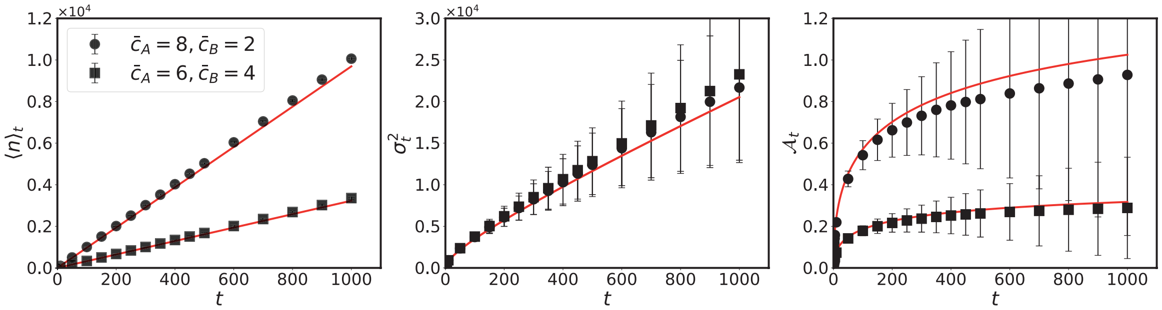

Figure 6. Janus catalytic particle: the mean number of reactive events $\langle n \rangle_t$, the corresponding variance σ_t^2, and the affinity $\mathcal{A}_t$ versus time t for the microscopic simulation with the multiparticle collision method. The dots and the squares are the simulation data of the multiparticle collision dynamics and the solid lines the theoretical results. The results are the average of 40 realizations and the error is given by the standard deviation.

Here also, the comparison between figures 5 and 6 shows that the time-dependent affinity $\mathcal{A}_t$ remains closer to its asymptotic value $\mathcal{A}_\infty$ in the reaction-limited regime than in the diffusion-limited regime, confirming the general behavior already observed in the spherical geometry. We also observe that the time-dependent affinity at early time is somewhat larger for the Janus particle that for the fully catalytic particle. The spherical catalytic particle yields product over its entire surface and this restricts the amount of reactant available to the surface. In contrast, there is a larger amount of reactant available on the noncatalytic portion of the Janus particle that can diffuse to the catalytic hemisphere and react. Thus, the catalytic portion of the Janus particle is more effective per unit catalytic area at yielding product than the spherical particle, and this may lead to a higher affinity at early time.

5. Conclusion and perspectives

In this paper, the finite-time fluctuation theorem of [17] has been investigated for the diffusion-influenced surface reaction $\mathrm{A} \rightleftharpoons \mathrm{B}$ on spherical and Janus catalytic particles. The finite-time rates of the forward and reverse reactions $\mathrm{A} \rightleftharpoons \mathrm{B}$ have been analytically calculated in both geometries by solving diffusion equations with the special boundary conditions obtained in [17]. These rates provide the time-dependent thermodynamic force or affinity driving the process away from equilibrium. This affinity converges towards its asymptotic value determined by the concentrations of the reacting species at the reservoir, as predicted by infinite-time fluctuation theorems. Using the time-dependent affinity, we can determine how the entropy production rate evolves in time during the counting of reactive events.

The results show that the affinity may take a much lower value at early time than its expected asymptotic value. The reason is that the affinity reaches its asymptotic value beyond the diffusion time characteristic of the reaction taking place on the catalytic particle. In the reaction-limited regime, this diffusive time is short, so that the affinity rapidly converges towards its asymptotic value. However, the diffusion time may be significantly longer in the diffusion-limited regime. For micrometric catalytic particles and small molecular-scale diffusing molecules whose diffusion coefficients in water are typically of the order of 10^{-9} m^2 s^{-1}, the convergence time (52) is of the order of milliseconds, which is short relative to macroscopic measurement times, hence justifying the use of the long-time limit.

Theoretical results for the spherical catalytic and Janus particles were compared with numerical simulations using two different methods: a random walk algorithm and an algorithm based on multiparticle collision dynamics. These systems were studied for diffusion-limited catalytic reactions as well as for reactions that lie in crossover regime between reaction- and diffusion-limited kinetics. In the diffusion-limited regime, the affinity takes an early-time value that is significantly smaller than its asymptotic value. In all cases theoretical and simulation results are in agreement.

In the three-dimensional geometries of the spherical and Janus catalytic particles, the convergence time does not depend on the distance between the catalytic surface and the reservoir where the concentrations of reacting species are fixed. This is no longer the case in the one-dimensional planar geometry, as we shall report in a future publication.

Acknowledgments

Financial support from the International Solvay Institutes for Physics and Chemistry, the Université libre de Bruxelles (ULB), the Fonds de la Recherche Scientifique—FNRS under the Grant PDR T.0094.16 for the project 'SYMSTATPHYS', the Belgian Federal Government under the Interuniversity Attraction Pole project P7/18 'DYGEST', and the Natural Sciences and Engineering Research Council of Canada is acknowledged.

Appendix A. Random walk simulation method and parameters

The system contains $i = 1, 2, ..., N$ particles moving in a cubic box of size $\mathscr{L}$ according to the Langevin stochastic differential equations $\mathrm{d}\mathbf{r}_i/\mathrm{d}t = \mathbf{v}_i(t)$ where the velocities are given by Gaussian white noises satisfying $\langle \mathbf{v}_i(t) \rangle = 0$ and $\langle \mathbf{v}_i(t) \otimes \mathbf{v}_j(t') \rangle = 2\, D\, \delta_{ij}\, \delta(t - t')\, \mathbf{1}$, expressed in terms of the diffusion coefficient D and 3×3 identity matrix $\mathbf{1}$. These equations are solved numerically by discretization into time steps $\Delta t = 0.001$. Initially, the cubic box is uniformly filled with 10^6 particles, so that the overall particle density is equal to $c_0 = 10^6/\mathscr{L}^3$. As the particles move into a sphere of radius $L < \mathscr{L}$ centered at the origin inside the box, they acquire a color A or B with the probabilities $\bar{P}_{\mathrm{A}} = \bar{c}_{\mathrm{A}}/c_0$ or $\bar{P}_{\mathrm{B}} = \bar{c}_{\mathrm{B}}/c_0 = 1 - \bar{P}_{\mathrm{A}}$. Simultaneously, particles crossing the surface $r = L$ are specularly reflected by the surface, so that the number of particles inside the sphere of radius L is constant and equal to $N = c_0 \times 4\pi L^3/3$. This determines the boundary values of the concentrations at $r = L$.

The color A or B of the moving particles changes upon their collision with the catalytic surface. The catalyst occupies a spherical domain of radius $R < L$ centered at the origin. The surface reaction is simulated according to the algorithm of [26]. Whenever the particle displacement $\mathbf{r}_i(t + \Delta t) - \mathbf{r}_i(t) = \boldsymbol{\Delta}_i(t)$ crosses the catalytic surface the moving particle changes its color with the probabilities $P_\pm = \kappa_\pm \sqrt{\pi \Delta t/D}$ and simultaneously its trajectory is specularly reflected by the surface. There is a chance that a particle hits the catalyst even if $\mathbf{r}_i(t+\Delta t)$ is located outside the spherical domain, since the particle might have crossed the catalyst surface twice during the time interval $[t, t+\Delta t]$. Thus, if $\mathbf{\Delta}_i(t)$ intersects the surface at two locations, the particle trajectory is reflected specularly at the first intersection point.

In the reported simulations, the following values are taken for the parameters: $\mathscr{L} = 10$, $L = 5$, $R = 0.5$, $D = 1$, $\bar{P}_{\rm A} = 10/19$, $\bar{P}_{\rm B} = 9/19$, and $c_0 = \bar{c}_{\rm A} + \bar{c}_{\rm B} = 10^3$. Time series with 10^6 data points have been computed for the number of reactive events during the time interval $10 \times \Delta t$ of the simulation. In equations (59) and (85), the given values of the concentrations have been determined from the mean numbers of particles of both species in the layer $L - \Delta r < r < L$ next to the reservoir (with $\Delta r = (L-R)/50 = 0.09$).

Appendix B. Microscopic simulation method and parameters

Here, we describe the hybrid molecular dynamics-multiparticle collision dynamics scheme and give the parameter values used in the simulations.

The Janus motor of radius $R = R_{\rm J} + \sigma = 5\,\sigma$ is placed in a cubic simulation box of linear length $\mathscr{L} = 50\,\sigma$ containing $N = N_{\rm A} + N_{\rm B} + N_{\rm S} = 2488\,439$ fluid particles with $N_{\rm A} + N_{\rm B} = N_{\rm S}$. The average densities of the fluid and reactive particles are $N/\mathscr{L}^3 \simeq 20$ and $c_0 = (N_{\rm A} + N_{\rm B})/\mathscr{L}^3 \simeq 10$, respectively. The construction of the Janus motor was described earlier [19]. It is made of 2681 beads randomly distributed in a sphere of radius $R_{\rm J} = 4\,\sigma$, where two beads within a distance $2\,\sigma$ are linked by a stiff spring with spring constant $k_{\rm s} = 50\,k_{\rm B}T/\sigma^2$, where $k_{\rm B}T$ is the thermal energy. The interaction between a motor bead and a fluid particle is given by a repulsive Lennard-Jones potential with interaction strength ϵ_α, $U_\alpha(r) = 4\,\epsilon_\alpha[(\sigma/r)^{12} - (\sigma/r)^6 + 0.25]$, which vanishes when $r > 2^{1/6}\sigma$. The interaction strengths are chosen as $\epsilon_{\rm A} = \epsilon_{\rm B} = 1.0$.

The nonequilibrium steady states discussed in the main text are established by considering a spherical region with radius $r = L = 24\,\sigma$ centered on the Janus motor. The region outside of $r = L$ is modeled as a reservoir with prescribed concentrations of A and B species, which can be controlled by changing the species type to A or B with probabilities $\bar{p}_{\rm A}$ and $\bar{p}_{\rm B}$ with $\bar{c}_{\rm A} = \bar{p}_{\rm A} c_0$ and $\bar{c}_{\rm B} = \bar{p}_{\rm B} c_0$. In the simulations we consider (a) $\bar{p}_{\rm A} = 0.8$ and $\bar{p}_{\rm B} = 0.2$ and (b) $\bar{p}_{\rm A} = 0.6$ and $\bar{p}_{\rm B} = 0.4$. Note that there is no change of species for inert S particles at the boundary $r = L$.

The dynamics of fluid particles is described by multiparticle collision dynamics comprising streaming and collision steps at discrete time intervals $\tau = 0.1\,t_0$. The collisions are carried out by first sorting the particles into a grid of cubic cells with linear size σ and the postcollision velocities of particle i in a cell ξ are given by $\mathbf{v}_i' = \mathbf{V}_\xi + \hat{\mathcal{R}}(\mathbf{v}_i - \mathbf{V}_\xi)$, where $\mathbf{V}_\xi$ is the center of mass velocity of particles in cell ξ and $\hat{\mathcal{R}}$ is a rotation operator about a random axis by an angle of 120°. Between two consecutive collisions, the system evolves by Newton's equation of motion with forces determined from the total potential energy of the system using a time step of $\delta t = 0.005\,t_0$. The common diffusion coefficient of fluid particles is found to be $D = 0.0596$. Simulation results are reported in dimensionless units where mass is in units of m, length in units of σ, energies in units of $k_{\rm B}T$ and time in units of $t_0 = \sqrt{m\sigma^2/k_{\rm B}T}$.

J. Stat. Mech. (2018) 123206

Appendix C. Discretization of the diffusion equations (74) and the boundary conditions (75)

The numerical method for solving equations (74) and (75) for $v_{kl}(r,t)$ is as follows. We suppose the diffusion coefficients and the rate constants are equal, $D \equiv D_{\rm A} = D_{\rm B}$ and $\kappa \equiv \kappa_{\pm}$ and, therefore, one obtains $v_l(r,t) \equiv v_{{\rm A}l}(r,t) = v_{{\rm B}l}(r,t)$. The discretized diffusion equation for $v_l(r,t)$ is

$$v_l(r,t+\Delta t) = \left[1 - 2\frac{D\Delta t}{\Delta r^2} - \frac{l(l+1)}{r^2}D\Delta t\right] v_l(r,t) + \frac{D\Delta t}{\Delta r^2}\left[v_l(r+\Delta r,t) + v_l(r-\Delta r,t)\right], \tag{C.1}$$

subjected to the boundary condition at $r = L$, $v_l(r=L,t) = 0$, and the boundary condition at $r = R$,

$$v_l(R,t) = \sum_{l'=0}^{\infty} \left(\tilde{\mathbf{M}}^{-1}\right)_{ll'} v_{l'}(R+\Delta r,t)\,, \tag{C.2}$$

where

$$\left(\tilde{\mathbf{M}}\right)_{ll'} = \left(1 + \frac{\Delta r}{R}\right)\delta_{ll'} + (2l+1)\,\frac{\kappa\Delta r}{D}\int_0^1 P_l(\xi)P_{l'}(\xi)\,{\rm d}\xi \tag{C.3}$$

with the Kronecker delta symbol $\delta_{ll'}$.

References

[1] Evans D J, Cohen E G D and Morriss G P 1993 *Phys. Rev. Lett.* **71** 2401
[2] Gallavotti G 1996 *Phys. Rev. Lett.* **77** 4334
[3] Kurchan J 1998 *J. Phys. A: Math. Gen.* **31** 3719
[4] Lebowitz J L and Spohn H 1999 *J. Stat. Phys.* **95** 333
[5] Jarzynski C 2011 *Annu. Rev. Condens. Matter Phys.* **2** 329
[6] Gaspard P 2004 *J. Chem. Phys.* **120** 8898
[7] Andrieux D and Gaspard P 2004 *J. Chem. Phys.* **121** 6167
[8] Andrieux D and Gaspard P 2006 *J. Stat. Mech.* P01011
[9] Derrida B, Douçot B and Roche P-E 2004 *J. Stat. Phys.* **115** 717
[10] Derrida B 2007 *J. Stat. Mech.* P07023
[11] Seitaridou E, Inamdar M M, Phillips R, Ghosh K and Dill K 2007 *J. Phys. Chem.* B **111** 2288
[12] Pressé S, Ghosh K, Phillips R and Dill K 2010 *Phys. Rev.* E **82** 031905
[13] Pressé S, Ghosh K, Lee J and Dill K 2013 *Rev. Mod. Phys.* **85** 1115
[14] Gaspard P 2013 *New J. Phys.* **15** 115014
[15] Bertini L, Sole A D, Gabrielli D, Jona-Lasinio G and Landim C 2015 *Rev. Mod. Phys.* **87** 593
[16] Andrieux D and Gaspard P 2008 *Phys. Rev.* E **77** 031137
[17] Gaspard P and Kapral R 2018 *J. Stat. Mech.* 083206
[18] Kapral R 2008 *Adv. Chem. Phys.* **140** 89
[19] Huang M-J, Schofield J, Gaspard P and Kapral R 2018 *J. Chem. Phys.* **149** 024904
[20] Bedeaux D, Albano A M and Mazur P 1976 *Physica* A **82** 438
[21] Malevanets A and Kapral R 1999 *J. Chem. Phys.* **110** 8605
[22] Malevanets A and Kapral R 2000 *J. Chem. Phys.* **112** 7260
[23] Gompper G, Ihle T, Kroll D M and Winkler R G 2009 *Adv. Polym. Sci.* **221** 1
[24] Tucci K and Kapral R 2004 *J. Chem. Phys.* **120** 8262
[25] Gaspard P and Kapral R 2018 *J. Chem. Phys.* **148** 134104
[26] Singer A, Schuss Z, Osipov A and Holcman D 2008 *SIAM J. Appl. Math.* **68** 844